IOP Publishing J. Phys.: Condens. Matter 38 (2026) 015702 https://doi.org/10.1088/1361-648X/ae24d6

Journal of Physics: Condensed Matter

Effect of partial oxidization on the transport in Fe/MgO/Fe tunnel junctions

RECEIVED
11 October 2025

REVISED
20 November 2025

ACCEPTED FOR PUBLICATION
26 November 2025

PUBLISHED
17 December 2025

Assaous Boubaker[1], **Baadji Nadjib**[2,*] **and Zanat Kamel**[3,*]

[1] Département de Physique & Laboratoire de Physique et Chimie des Matériaux, Faculté des Sciences, Université Mohamed Boudiaf, M'sila 28000, Algérie
[2] Département de Physique & Laboratoire de Physique des Matériaux et ses applications, Faculté des Sciences, Université Mohamed Boudiaf, M'sila 28000, Algérie
[3] Physics Laboratory at Guelma, Faculty of Mathematics, Computing and Materials Science, University 8 May 1945 Guelma, PO Box 401, Guelma 24000, Algeria
[*] Authors to whom any correspondence should be addressed.

E-mail: nadjib.baadji@univ-msila.dz and zanat.kamel@univ-guelma.dz

Keywords: Ab-initio quantum transport, TMR interfacial oxidation, incoherent scattering, vertex corrections

Abstract

The performance of Fe/MgO/Fe-based magnetic tunnel junctions is critically limited by interfacial oxidation; however, a complete theoretical framework capturing its complex role has been elusive. We developed an *ab initio* quantum transport approach that integrates the coherent potential approximation with vertex corrections to model substitutional disorder at oxidized Fe/MgO interfaces. Our model reveals that oxidation fundamentally reshapes spin-dependent transport, leading to a systematic suppression of the tunnel magnetoresistance (TMR) ratio, emergence of strong bias-voltage asymmetry, and crossover to negative TMR at high bias. Crucially, we demonstrate that the dominant transport mechanism in oxidized junctions is incoherent scattering, which is captured by vertex corrections that create disorder-assisted transport channels. This effect is particularly pronounced in asymmetric interfacial configurations, where it can paradoxically enhance the transmission. Furthermore, we show that increasing the MgO barrier thickness degrades TMR in highly oxidized junctions, as incoherent channels overwhelm coherent tunneling. Our work provides a predictive framework that moves beyond idealized models, establishing that vertex corrections are indispensable for accurately describing quantum transport in realistic disordered spintronic interfaces and guiding their design.

1. Introduction

Magnetic tunnel junctions (MTJs) with crystalline MgO barriers are fundamental building blocks in modern spintronics. Their ability to exhibit large tunnel magnetoresistance (TMR) has led to their widespread application in non-volatile memory (MRAM), data storage, and magnetic sensors [1–3]. Recently, renewed interest in their potential has been ignited by initiatives such as the US National Institutes of Health's Notice of Special Interest in 'Quantum Sensing Technologies in Biomedical Applications' [4]. For biomedical applications, such as magnetic biosensing and wearable medical devices, the key performance metrics are a wide dynamic range, high sensitivity, and superior noise performance [5]. The TMR ratio, defined as $\mathrm{TMR} = (I_\mathrm{P} - I_\mathrm{AP})/I_\mathrm{AP} \times 100\%$ (with I_P and I_AP being the currents in the parallel and antiparallel magnetic configurations of the electrodes, respectively), is a critical parameter that directly influences these metrics. The theoretical potential of Fe/MgO/Fe MTJs is immense. First-principles calculations based on coherent electron transport in ideal junctions predicted TMR ratios exceeding 1000% at room temperature [6, 7]. Following the seminal experimental reports of room-temperature TMR values up to 200% in epitaxial Fe/MgO/Fe structures [8, 9], progress has been steady, with record values now reaching approximately 600% at room temperature and over 1000% at low temperatures [10]. In pursuit of higher TMR ratios, significant research has been directed towards half-metallic ferromagnets like Heusler alloys with 100% spin polarization and exceptionally high TMR ratios [11, 12]. However, their experimental performance is severely limited by sensitivity to structural order and interfacial chemistry.

This work focuses on the well-controlled and technologically mature Fe/MgO systems to investigate universal interface challenges, such as oxidation.

However, a significant gap persists between these experimental achievements and the predicted theoretical limits. This discrepancy represents a central challenge in the field, hindering the full optimization of MTJ-based devices. The origins of this theory-experiment gap are attributed to defects and interfacial imperfections inherent to real-world fabrication. The structural characterization of the Fe/MgO interface remains controversial. For instance, surface x-ray diffraction (SXRD) studies by Tusche *et al* [13] revealed a partially oxidized Fe layer at both interfaces, with oxidation being more pronounced (up to 70%) at the Fe-on-MgO interface [14]. In contrast, x-ray photoelectron spectroscopy (XPS) studies at the Fe L_23 edge have been interpreted as evidence of a clean interface [15]. This disagreement underscores the critical role of growth conditions and characterization techniques; however, more recent O K-edge XPS studies provide clearer evidence of chemical shifts indicative of FeO formation [16–18].

It is important to note that the Fe/MgO and MgO/Fe interfaces inherently possess different oxidation potentials, primarily because of the different surface energies of MgO and Fe [19, 20]. This naturally leads to the asymmetric oxidation levels observed in prior experiments, where uncontrolled fabrication resulted in states such as 60% oxidation on one interface and 30% on the other [21], with Mössbauer spectroscopy revealing levels as high as 86% [22].

Theoretical efforts have focused on modeling specific defects to explain the suppressed TMR and specific transport features. The three most commonly considered defects are: (1) oxygen vacancies (V*O*) [23], (2) magnesium vacancies (V*Mg*) [24], and (3) interfacial oxidation [14, 25]. Oxygen vacancies, for example, have been shown to reduce the effective barrier height, bringing the theoretical decay of conductance with barrier thickness closer to experimental observations [26–28] . However, they often fail to fully account for the bias dependence of the TMR, asymmetry of the current–voltage ($I-V$) characteristics, severe suppression of the TMRs, and zero bias peculiarities. Furthermore, certain experiments report a sign change in TMR with applied bias, a phenomenon that is highly sample-dependent and eludes explanation by simple vacancy models [29]. Furthermore, real Fe/MgO interfaces exhibit atomic-scale mixing and roughness, which degrade TMR by disrupting coherent tunneling [30, 31]. While interfacial interdiffusion creates a magnetic dead layer [32], certain atomic configurations may have minimal impact [33]. Post-growth annealing enhances TMR by reducing roughness, creating a sharper interface [34]. A key future direction is to use computational models with a disordered interfacial layer to systematically separate the effects of chemical oxidation from topological disorder.

From a computational perspective, results are highly sensitive to the chosen method, particularly regarding the treatment of interface states near the Fermi level that dominate transport in thin barriers and the precise alignment of the MgO band edges with the Fe chemical potential (band offset) [25, 35–37]. To bridge this gap, a more comprehensive theoretical framework is required-one that can effectively handle the inherent disorder and randomness of the oxidized interface without relying on simplified, periodic defect supercells. In this study, we present such an approach. We employed the tight-binding linear muffin-tin orbital (TB-LMTO) method combined with the coherent potential approximation (CPA) [38] to explicitly model the substitutional randomness of oxygen and Fe atoms at the oxidized interface within an effective-medium framework. This allows for the first-principles calculation of the configurationally averaged Green's function of disordered interfaces. Furthermore, our method enables computationally efficient finite-bias quantum transport calculations. A key advancement of our approach is the systematic inclusion of vertex corrections within the Green's function formalism, which allows us to capture not only the coherent tunneling component but also the incoherent, diffusive scattering contributions that are crucial for accurately describing transport in disordered interfaces [39]. This comprehensive model provides a unified platform for reconciling a wide range of experimental data with theoretical predictions, ultimately guiding the design of next-generation high-performance MTJ sensors.

2. Computational and theoretical details

The electronic structure was calculated using the TB-LMTO method [38, 40]. Substitutional disorder was treated within the CPA, which provides an effective-medium framework for computing the configurationally averaged retarded Green's function. The electrodes were modeled as perfect crystals; consequently, all lead-related quantities, such as the self-energy, are non-statistical. The CPA formalism, initially introduced by Soven [41] and Taylor [42] and later developed mathematically by Velický [43], was employed. To ensure accuracy in transport properties, vertex corrections were incorporated into the calculation of the transmission coefficient and current under finite bias [39, 44]. These corrections partition the total transmission into coherent (secular) and incoherent (diffusive) components. Current–voltage characteristics were calculated using a rigid-band approximation. This approach has been demonstrated

to yield results in good agreement with fully self-consistent non-equilibrium Green's function calculations for Fe/MgO/Fe MTJs up to biases of 2 eV [37]. At the interfaces, oxidation of iron is modeled as a random process confined to the atomic layers at the Fe/MgO and MgO/Fe boundaries. We adopt a rigid lattice model, which assumes that the interfacial structure does not reconstruct upon oxidation and remains analogous to the atomic configuration of the fully oxidized interface [25, 36, 45]. We use the LSDA exchange correlation potential of [46] and the s, p, d basis sets to expand physical quantities. A fine k-mesh (40×40) is used to sample the transverse 2d Brillouin zone and to calculate transmission coefficients.

The aim of the present study is the development of an efficient way to compute the current-perpendicular-to-plane (CPP) transport properties of a substitutional disordered epitaxial tunnel junction with an *ab-initio* TB-LMTO-CPA framework [38]. We focus on the formulation of the rigid band approach for a finite applied bias within the so called vertex corrections arising in configuration averaging of a product of two Green functions [39, 43]. Our starting point is the one-particle electronic structure of a random configuration which can be described by the TB-LMTO method in the atomic sphere approximation [40, 46]. The electronic structure is expressed in terms of the tight-binding structure constants $\hat{S}$ and the energy-dependent potential function $\hat{P}$. The later is diagonal in sites and ℓ representation. The inclusion of the bias dependence in our calculation is done by replacing $\hat{P}$ by an energy- and a bias-dependent potential function:

$$\mathbf{P}(z, V) = \hat{P}\left(z + V\left(\vec{R}\right)\right), \tag{1}$$

where the vector $\vec{R}$ represents the atomic position and V the potential shift for each layer. Under an applied bias V, the internal electric field $\vec{E}(\vec{R})$ inside the metal is supposed to be zero due to the electronic screening, and a rigid shift of the energy levels is occurred, i.e,

$$V_p = \begin{cases} V & \forall \vec{R} \in \text{left metallic layer} \\ 0 & \forall \vec{R} \in \text{right metallic layer.} \end{cases}$$

The potential drop across the barrier, of length ℓ, is considered to be linear, and as consequence the internal electric field across the barrier is constant and is given by

$$\vec{E} = \frac{V}{\ell}\vec{k},$$

where $\vec{k}$ is a unit vector giving the direction of the growth of the junction. This leads to modify, the central quantity of the one-particle Green's function, namely the auxiliary Green's function matrix $\hat{g}$

$$\mathbf{g}\left(z, V_p\right) = \left[\mathbf{P}\left(z, V_p\right) - \hat{S}\right]^{-1}. \tag{2}$$

3. Geometrical and electronic structures

3.1. Junction geometry

The MTJ considered here is constructed of two semi-infinite disorder-free left (L) and right (R) lead of a body-centered cubic iron with a fixed in-plane lattice constant of $a = 2.866$ Å and limited by (001) surface. These leads are connected to (7)Fe/FeO_x/(n)MgO/FeO_y/(7)Fe active region (figure 1(a)), where the number in brackets indicates the number of layers and x and y are the degree of the iron oxidation. The (7)Fe layers are maintained at their bulk position (with an interplanar distance of 1.433 Å), while the adjacent oxidized Fe (FeO_x) layer is allowed to relax. Within this relaxed FeO_x layer, the Fe atoms are situated 1.7 Å below the z-position of the unrelaxed, adjacent (7)Fe layer, and the O atoms are positioned 0.2 Å below the z-position of the relaxed Fe plane. Regarding stacking: the Fe atoms of the (7)Fe layers are located directly on top of the O atoms of the FeO_x layer, and the interfacial Fe atoms of the FeO_x layer are located directly on top of the O atoms of the MgO barrier, maintaining a Fe–O distance of 2.35 Å across the interface.

For the calculation of the transmission coefficients and TMR, the magnetizations of the left and right (7)Fe layers are aligned in either a parallel or an antiparallel configuration relative to each other. To simulate the partially oxidized interface, a fraction of the oxygen atoms were replaced with vacant lattice sites. These vacancies are represented by 'empty spheres' (ES), leading to the formal occupation formula O_xES_{1-x}. This empty sphere and the oxygen atoms have the same Wigner radius. The first MgO layer is at 2.25 Å and the inter-planar distance in MgO is 2.15 Å. Two kind of empty spheres are added to fill

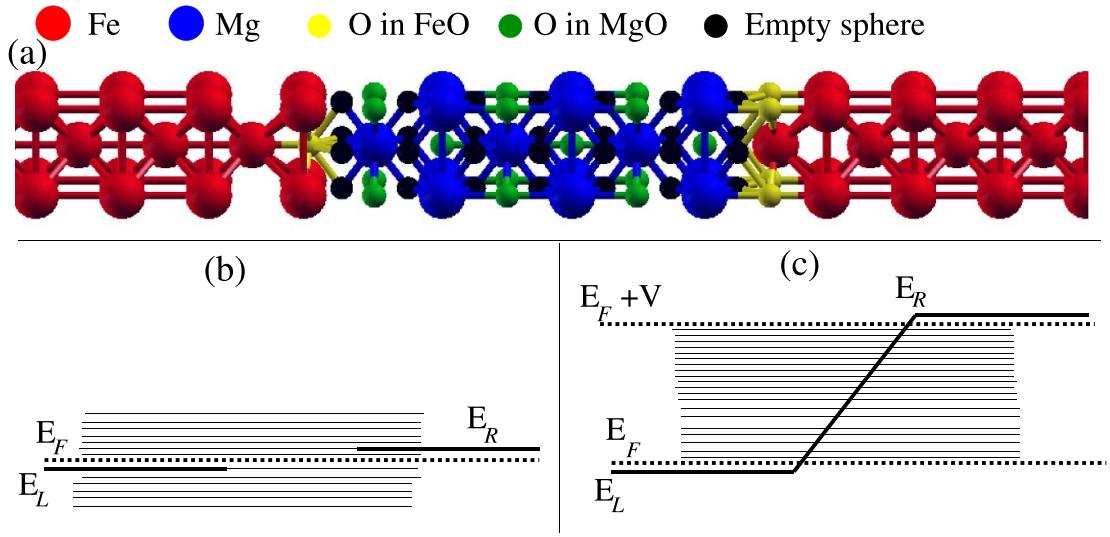

Figure 1. Active region and schematic potential drop through the junction: (a) active region showing the relative position of the Fe/FeO/6MgO/FeO/Fe Magnetic junction: the oxygen site in FeO layer is constructed by x O and $1-x$ empty spheres with the same Wigner radius, the distribution of O in this layer is assumed to be random. (b) Schematic for energy levels used to calculate the transmission coefficients for zero bias, with $E_F = (E_L + E_R)/2$. (c) Energy levels inside the bias window: The right lead is shifted by the bias (V) and linear drop of the potential through the junction is assumed.

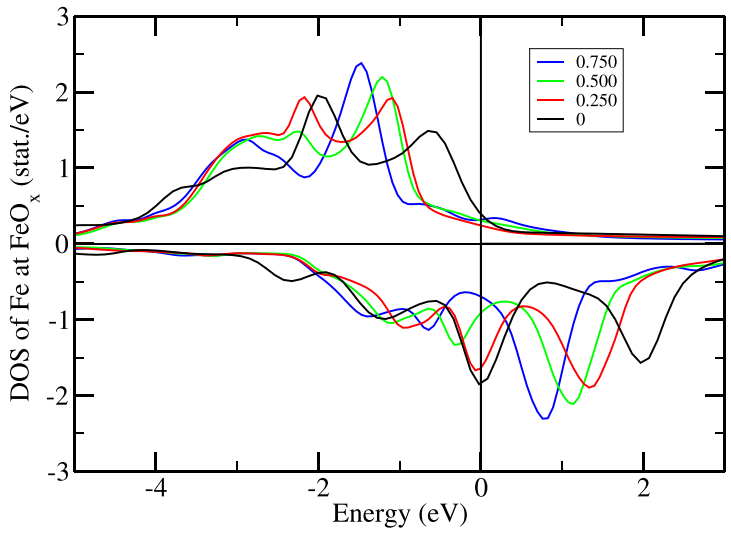

Figure 2. Total density of states of Fe at the interface FeO_x for different O concentrations: $x = 0$ black, $x = 0.25$ red, $x = 0.50$ green and $x = 0.75$ blue.

the interstitial space one type between the FeO and the MgO and the second between the MgO layers of radius 0.93 Å and 0.96 Å, respectively. The Wigner radii are 1.41, 0.96, and 1.17 Å for Fe, O, and Mg, respectively. Such geometry is identical to that of Heiliger *et al* [25] supported by x-ray absorption spectroscopy (XAS) measurements [14].

3.2. Electronic structure

To understand the effect of partial oxidation on electronic transport in Fe/MgO/Fe MTJs, it is necessary to study firstly its impact on the electronic structure. Figure 2 presents the atomically resolved density of states (DOS) of iron atoms at the oxidized interface (FeO_x) for different oxygen concentrations (x), from a clean interface ($x = 0$) to a partially oxidized one ($x = 0.75$).

The minority-spin channel exhibits more significant modifications than the majority-spin channel. A key change is the shift of peaks to lower energies with increasing x. Notably, the interface state peak located at the Fermi level (E_F) in the clean junction-previously discussed in reference [37, 47, 48]-shifts away from E_F and broadens. This is a consequence of p-d hybridization between the Fe d-orbitals and O p-orbitals. Furthermore, an unoccupied peak in minority spin, initially located 2 eV above E_F moves

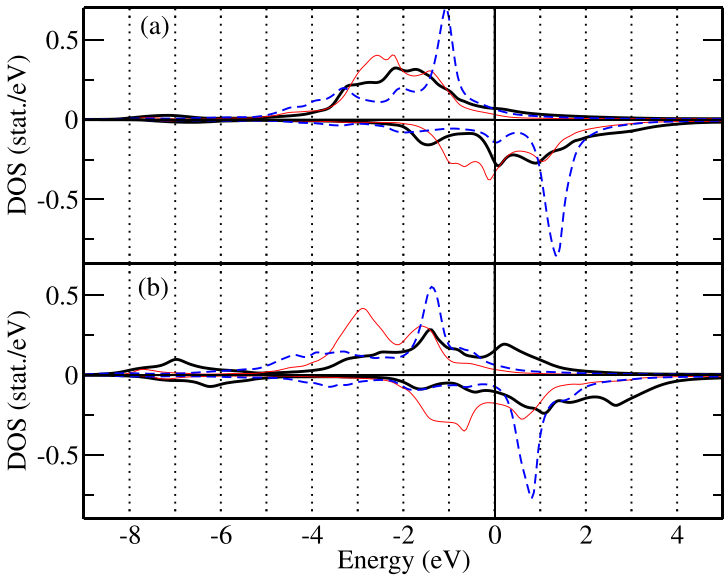

Figure 3. The orbital projected density of states for 3d-Fe at the interface FeO_x in Fe/FeO_x/MgO/Fe junctions for two different value of x: (a) $x = 0.25$ and (b) $x = 0.75$. d^2 orbital is presented by a (black) Thick solid line, d^1 (red) thin solid line and d^0 (or d_{z^2}) (blue) dashed line.

closer to the Fermi level as the oxidation level, x, increases. This shift of d-orbital towards lower energies leads to an augmentation of the occupation in d-minority band and a reduction of the magnetic moment at the interface, passing from 2.80 μ_B for a clean interface ($x = 0$) to 2.16 μ_B for fully oxidized layer ($x = 1$).

To gain deeper insight into the effect of partial oxidation, we present the d-orbital-resolved DOS of Fe atoms at the oxidized interface (FeO_x) for two oxygen concentrations, $x = 0.25$ and $x = 0.75$ (figure 3). In addition to the peak shifts discussed previously, the orbital character of the states at the Fermi level evolves with x. We focus particularly on the Δ_1 symmetry contribution.

The spectral weight of the d_{z^2} orbital ((blue) dashed line in figure 2), which constitutes the Δ_1 state, increases at the Fermi level with higher oxygen concentration. Consequently, the half-metallic character of the Δ_1 band-present in the ideal junction -is lost at the partially oxidized interface (FeO_x). A high TMR ratio relies on the selective presence of the Δ_1 band only in the majority spin channel as established in prior works [6, 49]. The interfacial oxygen hybridizes with Fe, inducing a significant Δ_1 contribution in the minority spin channel at the Fermi level, as well, and hence a reduction of the TMR ratio observed in thick junctions.

4. Zero-bias transmission coefficient: ballistic vs diffusive

We now investigate the effect of partial oxidation at the interface on the transport properties. We start by presenting the calculated transmission coefficients for Fe/FeO_x/MgO/FeO_y/Fe(001) junctions with three interface configurations: clean ($x = y = 0$), symmetrically oxidized ($x = y = 0.25$), and asymmetrically oxidized ($x = 0.25$, $y = 0.75$), as shown in figure 4. These values are representative of ideal (0%), low (25%) and high (75%) oxidation levels.

In the parallel configuration of the clean junction ($x = y = 0$), a sharp interface state resonance at the Fermi level (E_F) produces a dominant peak in the minority-spin transmission. In contrast, the antiparallel configuration exhibits a profound suppression of transmission, with both spin channels reduced by two orders of magnitude near E_F. The transmission in the antiparallel (AP) configuration remains lower than in the parallel (P) configuration for energies up to 1.5 eV above E_F. This results in a positive TMR for accessible applied bias voltages.

However, the introduction of partial oxidation shifts the interface states responsible for these resonant features away from the Fermi level. This shift reduces the transmission in the parallel configuration for both symmetric and asymmetric junctions in the vicinity of E_F (as discussed in section 3.2 on the DOS). Concurrently, in the antiparallel configuration, the transmission coefficient increases due to the enhanced Δ_1 contribution in the minority spin channel. The combination of reduced parallel transmission and increased antiparallel transmission leads to a net decrease in the TMR ratio.

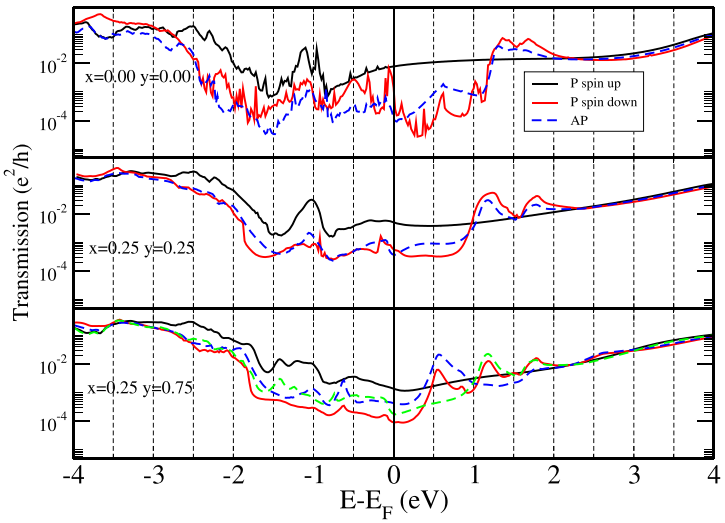

Figure 4. Calculated spin-resolved transmission coefficients for Fe/FeO_x/(4)MgO/FeO_y/Fe(001)for ideal junction $x = y = 0$, symmetrically oxidized interfaces $x = y = 0.25$ and asymmetrically oxidized interfaces $x = 0.25, y = 0.75$, for both parallel and antiparallel configurations. For parallel (antiparallel) configuration, the majority contribution is presented by black solid lines (dashed green lines) and the minority spin by red solid lines(blue dashed lines).

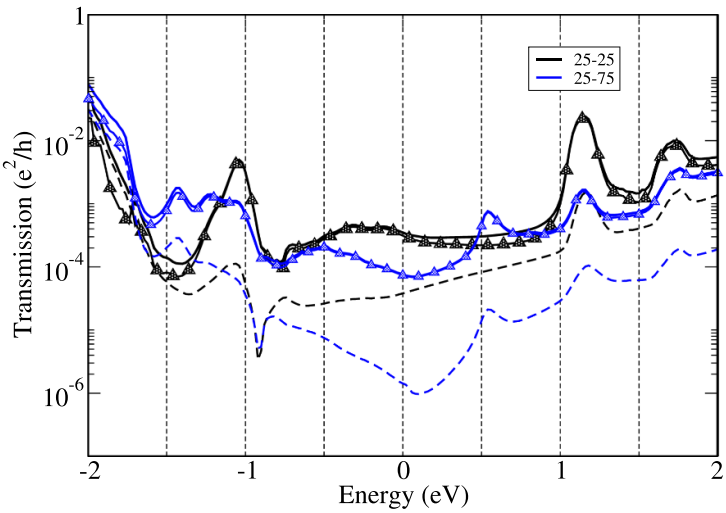

Figure 5. Decomposition of the total transmission coefficient (solid lines) into coherent (dashed lines) and uncoherent (triangles) for symmetric junctions Fe/FeO_x/MgO/FeO_x/Fe with $x = 25\%$ (black) and asymmetric junctions Fe/FeO_x/MgO/FeO_y/Fe with $x = 25\%, y = 0.75\%$ (blue).

In the asymmetrically oxidized junction, the antiparallel (AP) transmission exceeds the parallel (P) transmission at approximately 0.7 eV above E_F- an energy corresponding to an experimentally accessible bias voltage. This inversion of the dominant transmission channel results in a negative TMR, a finding we will elaborate on in the next section and one that is consistent with experimental observations. The crossover energy where AP transmission surpasses P transmission is attributed to the peak above the Fermi level associated with the Δ_1 state, as discussed in the previous DOS analysis. In addition, the spin degeneracy in the transmission is lifted for the asymmetric junction in the antiparallel configuration.

To gain deeper insight into the transmission mechanisms, we decompose the total transmission into its coherent and incoherent contributions, as defined by equations (A.16) and (A.17) in the appendixes and illustrated in figure 5. The coherent transmission, represented by dashed lines in figure 5, is expressed in terms of the averaged auxiliary Green's function as

$$T_{coh}\left(\mathbf{k}_{\parallel}, E, V\right) = \lim_{\delta \to 0^+} \frac{1}{2} Tr\left[B_1(E)\,\overline{\mathbf{g}}(z_+)\,B_N(E)\,\overline{\mathbf{g}}(z_-) + B_1\overline{\mathbf{g}}(z_-)\,B_N(E)\,\overline{\mathbf{g}}(z_+)\right] \tag{3}$$

and represents secular (ballistic) tunneling through the effective medium described by the CPA. This contribution decreases with increasing oxidation and provides only a minor contribution to the total

transmission. In contrast, the incoherent (diffusive) contribution, quantified by vertex corrections, arises from disorder scattering and is the dominant mechanism for electronic transport in the oxidized junctions. In the Fe/FeO_x/MgO/FeO_y/Fe system, where interfacial oxidation is randomly distributed, the standard CPA alone fails to account for the full impact of diffusive scattering. Vertex corrections rectify this by incorporating the statistical correlations between scattering events from the retarded and advanced Green's functions, following the same derivation done by Carva *et al* [39]

$$\langle \mathbf{g}(z_+)\, B(a)\, \mathbf{g}(z_-)\rangle = \bar{\mathbf{g}}(z_+)\, B(a)\, \bar{\mathbf{g}}(z_-) + \bar{\mathbf{g}}(z_+)\, \Gamma(z_+, z_-)\, \bar{\mathbf{g}}(z_-) \neq \bar{\mathbf{g}}(z_+)\, B(a)\, \bar{\mathbf{g}}(z_-) \tag{4}$$

These correlations capture the essential physics of quantum interference induced by oxidation-induced disorder. Vertex corrections are particularly critical in asymmetric configurations (e.g. the '$x = 0.25 - y = 0.75$' interface). Counter-intuitively, strong disorder in these junctions leads to higher transmission compared to symmetric ones at energies around 0.5 eV above E_F (see figure 5). This effect arises from disorder-assisted transport channels, which are entirely missed by the averaged CPA Green's function but are captured by the vertex corrections. Thus, including vertex corrections is indispensable for accurately modeling quantum transport across realistic disordered interfaces. They provide a complete framework that can predict the critical, and often counterintuitive, role of disorder. This is particularly relevant for spintronics, where controlled oxidation can tailor conductance, as vertex corrections quantitatively explain how disorder can enhance -rather than simply degrade- quantum tunneling.

5. Impact of interfacial oxidation on TMR

Having established the impact of partial oxidation on the zero-bias transmission coefficient, we now extend our analysis to examine its effect on the bias voltage dependence of the TMR in the linear response regime. We consider junctions with varying degrees of oxidation for both symmetric and asymmetric interface configurations. The results are presented in figures 6 and 7, respectively.

In symmetrically oxidized junctions ($x = y$), increasing the oxidation level leads to a systematic suppression of the TMR ratio (see figure 6). This is accompanied by a broadening of the TMR peak and a partial suppression of the zero-bias anomaly, indicating enhanced scattering and a modification of the spin-polarized interface states. A pivotal finding is the emergence of negative TMR at higher bias voltages; for instance, at a 75% oxidation level, the TMR inverts its sign around 0.5 V which is close the value observed experimentally [29]. This sign inversion, which our calculations trace directly to the behavior of the underlying transmission coefficients, signifies a fundamental crossover in transport regime where the junction conductance in the antiparallel magnetic configuration surpasses that in the parallel configuration.

The role of interfacial disorder and asymmetry is further elucidated by examining asymmetric junctions ($x \neq y$). These structures successfully replicate all key observations from the symmetric case-including TMR suppression, peak broadening, and negative TMR- but with the addition of a pronounced bias-voltage asymmetry. This asymmetry is characterized by a systematic shift of the maximum TMR value away from zero bias, typically toward negative potentials (see figure 7).

The fact that these most of the observed anomalies and complex phenomena are reproduced in asymmetric junctions confirms that the dominant effects of oxidation are localized at the individual interfaces rather than being a consequence of the global symmetry of the system. Consequently, localized states at each interface create a spin-polarized tunneling imbalance that is highly sensitive to bias direction.

Specifically, we find that the TMR changes sign at a bias voltage of 0.6 V for a symmetric junction ($x = y$) and at 0.5 V when one interface is 75% oxidized and the other is 12.5% oxidized (an asymmetric junction, $x \neq y$). These values are in good agreement with the work of Kalitsov *et al* [29], who observed a TMR sign change at approximately 0.7 V. Furthermore, their model for an ideal junction also predicts TMR asymmetry and a sign change at a bias of about 1 V. This critical bias voltage for the TMR sign change can be even lower in intentionally oxidized interfaces. For instance, Tiusan *et al* [50] demonstrated a sign change at approximately 0.2 V in a Fe/FeO/MgO/Fe junction. Regarding the magnitude of TMR, the highest value reported at low temperature is 1000% (which we can obtain for example by taking $x = 0.125$ and $y = 0.25$). For practical Yuasa-type junctions, which exhibit TMR saturation at MgO thicknesses of around 2 nm (approximately 8 to 9 mono-layers), the TMR ratio is typically on the order of 250%. A smaller value (110 %) was reported for Fe/FeO/MgO/Fe (see [51]). These values can be obtained in our calculation by changing x and y. for symmetric junction an oxidation of 50% leads to a TMR (at zero bias) of the order of 200%(164%). While for asymmetric junction a same value is

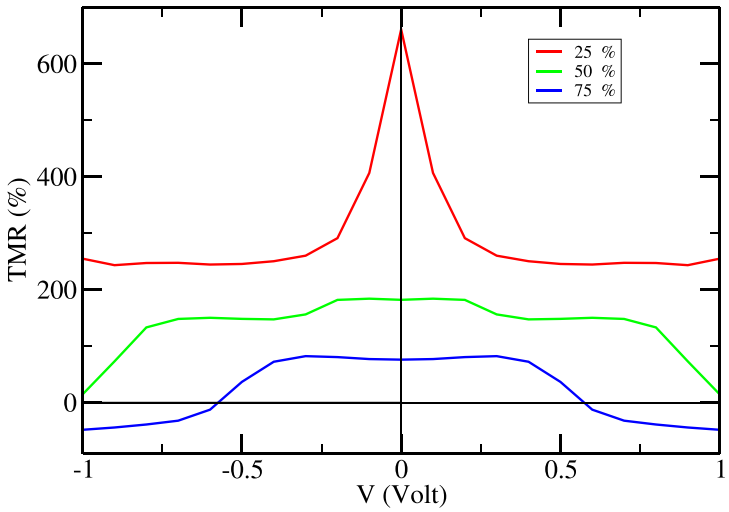

Figure 6. Variation of the tunnel magnetoresistance (TMR) for symmetric junctions (Fe/FeO_x/MgO/FeO_x/Fe) with different oxidation states: for $x = 0.25$ (red), $x = 0.5$ (green), and $x = 0.75$ (blue).

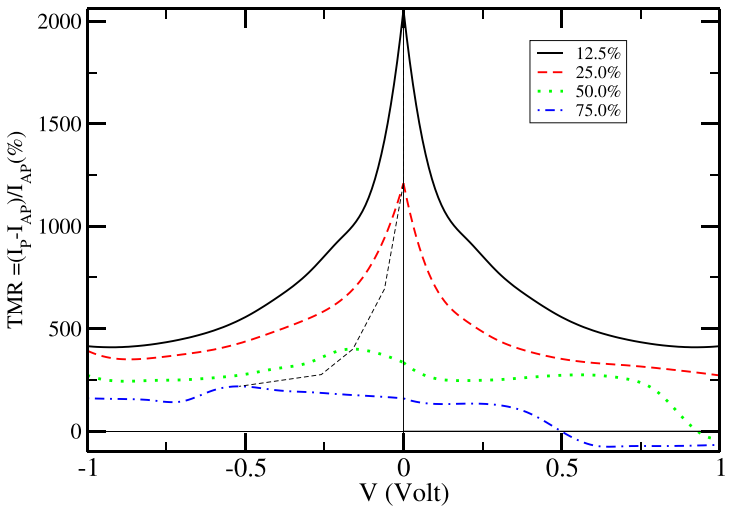

Figure 7. Variation of the TMR for asymmetric junctions Fe/FeO_x/MgO/FeO_y/Fe where x kept fix ($x = 0.125$) and y was varied at the other interface: $y = 0.125$ (black) solid line, $y = 0.25$ (red) dashed line, $y = 0.5$ (green) dotted line and $x = 0.75$ (blue) dashed-dotted line.

obtained for $x = 0.125$ and $y = 0.75$ and it is further reduced to 71% for $y = 0.875$. If we increase the oxidation on the other side ($x = 0.25$) we get TMR of 150% in good agreement with previously cited values. The TMR value becomes 296% for $x = 0.25$ and $y = 0.50$ and 335% for $x = 0.125$ and $y = 0.50$. From these values one can conclude that MTJ grown by molecular beam epitaxy have better interface with less oxidation and thus Higher TMR. While other preparation methods induces interface with higher oxidation interface and thus lower TMR.

The physical origin of these effects can be understood through the interplay coherent and diffusive transport. The CPA can capture the coherent (secular, ballistic) tunneling through the disorder-averaged effective medium, a component that diminishes with oxidation even in the presence of disorder but it misses uncoherent (diffusive) tunneling quantified by vertex corrections. These corrections capture the quantum interference effects from scattering off the oxidation-induced disorder, creating disorder-assisted transport channels.

Our approach moves beyond idealized ballistic models and the standard mean-field CPA. By including vertex corrections to capture the essential physics of disorder, it reproduces key experimental observations in Fe/MgO/Fe junctions, including TMR suppression, peak broadening, a partially suppressed zero-bias anomaly, and negative, asymmetric bias dependence.

This is indispensable for applications where controlled oxidation is intentionally used to tailor device characteristics, as it quantitatively explains how interfacial disorder can be engineered to induce specific functional behaviors, such as bias asymmetry and negative TMR, rather than being viewed solely as a performance-degrading factor.

6. Thickness dependence of the TMR

Finally, we investigate how interfacial oxidation affects the dependence of TMR on MgO barrier thickness, aiming to reproduce its experimentally observed saturation [9]. Figure 8 presents the zero-bias TMR for junctions with a pristine bottom interface and a top interface with varying oxidation levels. For low oxidation (near-ideal junctions), the TMR increases with barrier thickness, consistent with the theoretical model of coherent tunneling and enhanced spin filtering of Δ_1 symmetry electrons in crystalline MgO. Indeed, the coherent tunneling model, which is the fundamental mechanism in ideal Fe/MgO/Fe junctions, states that the decay rate of electron states through the MgO barrier depends critically on their band symmetry [49]. Specifically, the Δ_1 state has a much slower decay rate (κ_1) than the Δ_5 state (κ_2), that is $\kappa_1 < \kappa_2$. In Fe electrodes, the majority-spin electrons at the Fermi level predominantly have Δ_1 character, whereas the minority-spin electrons primarily have Δ_5 character. The MgO barrier thus acts as a symmetry-based spin filter, which is highly transparent to Δ_1 states and opaque to Δ_5 states. As the barrier thickness (d) increases, the filtering effect is enhanced. The upward TMR trend for the 1% oxidation junction is shown in figure 8, signals this coherent tunneling, where the TMR is expected increase and scale as $e^{(\kappa_2-\kappa_2)d}$ [18, 52]. However, for oxidation levels exceeding 37%, this trend breaks down; the TMR magnitude saturates and no longer increases with thickness. At high oxidation levels (75%), a pronounced degradation is observed, characterized by a significant decrease in TMR with increasing thickness. This thickness-dependent degradation is attributed to the increased dominance of diffusive scattering processes at the oxidized interface, which introduce significant vertex contributions and a mixture of d-band characters into the tunneling transport. These incoherent mechanisms compete with and ultimately overwhelm the coherent tunneling channel, an effect that becomes more detrimental as the barrier thickness increases.

In summary, the role and impact of interfacial oxidation, as detailed in our study of the Fe/FeO_x/MgO/FeO_y/Fe system, is a universal consideration in the design and performance of MTJs with diverse material stacks. This generalizability stems from two fundamental factors: the thermodynamic tendency of most transition metal (TM) electrodes to oxidize and the extreme sensitivity of spin-dependent tunneling to the atomic-scale structure and chemistry of the ferromagnet/barrier interface. The formation of interfacial oxides is highly dependent on deposition conditions (e.g. oxygen partial pressure, temperature) and the relative oxygen affinity of the electrode materials. Uncontrolled oxidation often degrades MTJ performance by disrupting the coherent tunneling mechanism. This occurs through the introduction of disorder and spin-scattering sites at the interface, which compromise the orbital symmetry filtering effect crucial for high TMR in crystalline systems such as Fe/MgO/Fe. Furthermore, many TM oxides (e.g. FeO, CoO, NiO) are antiferromagnetic or magnetically disordered, forming so-called 'magnetically dead layers' that quench spin polarization at the interface and severely degrade spin filtering. Evidence of this detrimental effect is widespread. For instance, in MTJs with a Heusler alloy Fe_2CrSi (FCS) electrode, a significantly reduced TMR ratio of only 2.5% was directly attributed to interfacial oxidation of the FCS layer [53]. Conversely, positive outcomes can be achieved by suppressing oxidation.

A recent study on Mn_3Ge/MgO MTJs demonstrated that preventing the oxidation of Mn at the interface was key to achieving a substantially enhanced TMR ratio [54]. However, it is critical to note that the presence of an interfacial oxide is not inherently detrimental. Our work shows that controlled oxidation can be leveraged to engineer novel functionalities. This aligns with theoretical predictions that a precisely defined oxidized interface can lead to quantum-well states in the electrode, giving rise to a resonance-enhanced TMR effect, as proposed for systems like Al/Fe/FeO/MgO/Fe [55]. Therefore, the central challenge has shifted from mere prevention to precision engineering, which involves understanding and controlling the thickness, stoichiometry, and magnetic structure of the interfacial oxide layer.

Ultimately, although the specific chemical and magnetic nature of the interfacial oxide varies with the electrode material (e.g. FeO_x in our study vs. MnO_x in Mn_3Ge or complex oxides in Heusler alloys), the fundamental principle holds: the interface is an active component. The findings of our study on the Fe/FeO_x system provide a framework for understanding how interfacial oxidation impacts spin transport, a concept directly applicable to MTJs based on other ferromagnetic electrodes (e.g. CoFeB, Heusler alloys) or alternative barrier oxides (e.g. $MgAl_2O_4$, TiO_2). The key is to tailor the growth and processing conditions to either suppress unwanted oxidation or harness it in a controlled manner for enhanced performance.

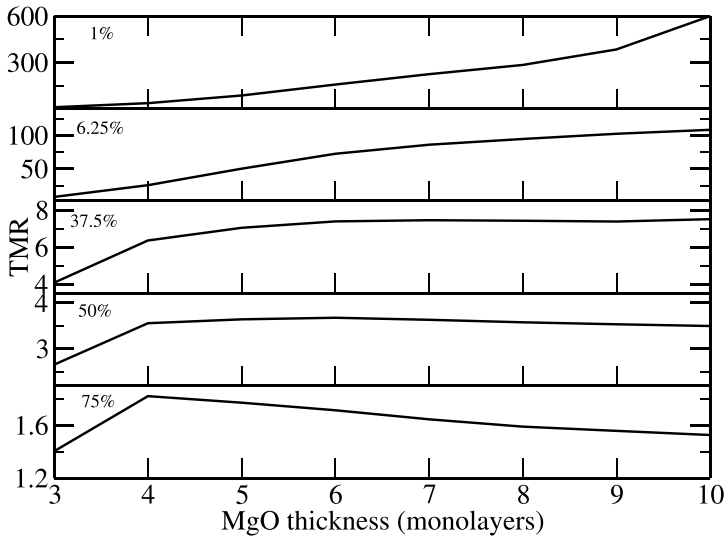

Figure 8. Variation of the TMR as function of the number of MgO layers for different value of oxidation (x) at one interface while the other is kept clean (Fe/FeO_x/MgO/Fe).

7. Conclusions

In conclusion, we presented a comprehensive computational study that resolves the intricate effects of interfacial oxidation on quantum transport in Fe/MgO/Fe MTJs. By employing a TB-LMTO-CPA methodology augmented with vertex corrections, we moved beyond the standard mean-field treatment of disorder to capture the essential physics of coherent scattering and quantum interference.

Our key findings are threefold, (i) TMR suppression and functional alteration: interfacial oxidation systematically degrades the TMR ratio and qualitatively alters its behavior, inducing bias-voltage asymmetry and, under certain conditions, a sign inversion to negative TMR. This inversion signifies a crossover, where the antiparallel configuration becomes more conductive than the parallel configuration. (ii) Critical role of vertex corrections: the standard CPA, which describes coherent tunneling through an effective medium, fails to account for the full impact of disorder. We have shown that the inclusion of vertex corrections is essential because they quantify the dominant incoherent (diffusive) contribution to transport. These corrections reveal the existence of disorder-assisted transport channels, which explains the counterintuitive enhancement of transmission in asymmetric junctions and the prevalence of negative TMR. (iii) Implications for device design: the localization of these effects at individual interfaces, confirmed by studies on asymmetric junctions, provides critical insights for device engineering. This implies that the electronic properties can be tailored by independently controlling the oxidation profile at each interface. Moreover, the finding that TMR degrades with barrier thickness in highly oxidized junctions highlights the competition between coherent tunneling and incoherent scattering, guiding the optimization of barrier properties.

This study bridges a significant gap between idealized theoretical models and experimental reality. By providing a unified platform that accurately captures the impact of interfacial disorder, our framework offers a powerful tool for predicting and engineering the transport properties of next-generation spintronic devices, in which controlled oxidation can be leveraged as a design parameter rather than merely a source of degradation.

Data availability statement

All data that support the findings of this study are included within the article (and any supplementary files).

Conflict of interest

No conflict of interest/Competing interests

Appendix

A.1. Surface Green's function

Suppose the magnetic multilayers system consists of non-random semi-infinite left (L) and right (R) leads sandwiching a trilayer consisting of a u left layers and v right layers of a magnetic slabs and w nonmagnetic layers as spacer. In the Tight-binding LMTO approach the auxiliary Green's function is expressed in terms of the structure constants $S^{LL'}_{RR'}$ and potential function P^L_R as

$$g\left(\mathbf{k}_{\parallel},z\right)=\left[P(z)-S\left(\mathbf{k}_{\parallel}\right)\right]^{-1} \tag{A.1}$$

where

$$P^L_R(z)=\frac{z-C_{RL}}{\Delta_{RL}+\left(\gamma_{RL}-\beta_L\right)\left(z-C_{RL}\right)}. \tag{A.2}$$

Assuming that the active part of the multilayer system consist of $N=u+v+w$ layers and that the physical properties of all leads layers are identical, so-called embedding potentials Γ [38] can be defined for the first $p=1$ and the last layer $p=N$ are given by

$$\Gamma\left(\mathbf{k}_{\parallel},z\right)=\begin{cases} S^{\beta}_{1,0}\left(\mathbf{k}_{\parallel}\right)\mathbf{G}_L\left(\mathbf{k}_{\parallel},z\right)S_{0,1}\left(\mathbf{k}_{\parallel}\right) & p=1 \\ S^{\beta}_{N,N+1}\left(\mathbf{k}_{\parallel}\right)\mathbf{G}_R\left(\mathbf{k}_{\parallel},z\right)S_{N+1,N}\left(\mathbf{k}_{\parallel}\right) & p=N \\ 0 \end{cases} \tag{A.3}$$

where $\mathbf{G}_{L(R)}$ is the bulk green function for left(right) lead. The auxiliary Green function, now, reads

$$g\left(\mathbf{k}_{\parallel},z\right)^{-1}_{p,p}=\begin{cases} P_1(z)-S\left(\mathbf{k}_{\parallel}\right)-\Gamma_1\left(\mathbf{k}_{\parallel},z\right) & p=1 \\ P_p(z)-S\left(\mathbf{k}_{\parallel}\right) & 2\leqslant p\leqslant N-1 \\ P_N(z)-S\left(\mathbf{k}_{\parallel}\right)\Gamma_N\left(\mathbf{k}_{\parallel},z\right) & p=N \end{cases}$$

and the off-diagonal elements are

$$\left[g\left(\mathbf{k}_{\parallel},z\right)\right]^{-1}_{p,q}=-\hat{S}_{p,q}\left(\mathbf{k}_{\parallel}\right)\delta_{p,q\pm1}. \tag{A.4}$$

To include the bias in this approach we simply consider that the left leads and the first u layer are shifted in energy by the bias V and that in the w nonmagnetic layer the potential drops linearly such, if the u^{th} left layer position is $\vec{r}_L$ and the first magnetic left layer's position is $\vec{r}_R$, the potential drop for each nonmetallic layers is given by:

$$V_p=\begin{cases} V & p\leqslant v \\ \dfrac{\left(\vec{R}_p-\vec{r}_R\right).\vec{k}}{\left(\vec{r}_L-\vec{r}_R\right).\vec{k}}V & v<p\leqslant v+w \\ 0 & p>v+w \end{cases}. \tag{A.5}$$

This leads to replace the potential function P by

$$\mathbf{P}_{RL}(z,V)=P_{RL}\left(z+V_p\right)=\begin{cases} \dfrac{z+V-C_{RL}}{\Delta_{RL}+\left(\gamma_{RL}-\beta_L\right)\left(z+V-C_{RL}\right)} & p_R\leq v \\ \dfrac{z+\dfrac{\left(\vec{R}_p-\vec{r}_R\right).\vec{k}}{\left(\vec{r}_L-\vec{r}_R\right).\vec{k}}V-C_{RL}}{\Delta_{RL}+\left(\gamma_{RL}-\beta_L\right)\left(z+\dfrac{\left(\vec{R}_p-\vec{r}_R\right).\vec{k}}{\left(\vec{r}_L-\vec{r}_R\right).\vec{k}}V-C_{RL}\right)} & v<p_R\leq v+w \\ \dfrac{z-C_{RL}}{\Delta_{RL}+\left(\gamma_{RL}-\beta_L\right)\left(z-C_{RL}\right)} & p_R>v+w \end{cases} \tag{A.6}$$

and the embedded potential is replaced by

$$\mathbf{\Gamma}_p\left(\mathbf{k}_\parallel, z, V\right) = \begin{cases} S^{\beta}_{1,0}\left(\mathbf{k}_\parallel\right)\mathbf{G}_L\left(\mathbf{k}_\parallel, z+V\right)S^{\beta}_{0,1}\left(\mathbf{k}_\parallel\right) & p=1 \\ S^{\beta}_{N,N+1}\left(\mathbf{k}_\parallel\right)\mathbf{G}_R\left(\mathbf{k}_\parallel, z\right)S^{\beta}_{N+1,N}\left(\mathbf{k}_\parallel\right) & p=N \\ 0 \end{cases}. \tag{A.7}$$

The auxiliary Green's function is now written as

$$\left[\mathbf{g}\left(\mathbf{k}_\parallel, z, V\right)\right]^{-1}_{p,p} = \begin{cases} \mathbf{P}_1(z,V) - \hat{S}\left(\mathbf{k}_\parallel\right) - \mathbf{\Gamma}_1\left(\mathbf{k}_\parallel, z, V\right) & p=1 \\ \mathbf{P}_p(z) - \hat{S}\left(\mathbf{k}_\parallel\right) & 1<p<N \\ \mathbf{P}_N(z,V) - \hat{S}\left(\mathbf{k}_\parallel\right) - \mathbf{\Gamma}_N\left(\mathbf{k}_\parallel, z, V\right) & p=N \end{cases} \tag{A.8}$$

and the off-diagonal elements are

$$\left[\mathbf{g}\left(\mathbf{k}_\parallel, z, V\right)\right]^{-1}_{p,q} = -\hat{S}_{p,q}\left(\mathbf{k}_\parallel\right)\delta_{p,q\pm1}. \tag{A.9}$$

Furthermore, the transmission coefficients can be expressed as

$$T\left(\mathbf{k}_\parallel, E, V\right) = \lim_{\delta\to0^+}\frac{1}{2}Tr\left[B_1(E)\,\mathbf{g}(z_+)\,B_N(E)\,\mathbf{g}(z_-) + B_1(E)\,\mathbf{g}(z_-)\,B_N(E)\,\mathbf{g}(z_+)\right] \tag{A.10}$$

where B self-energy is the imaginary part of the embedded potential $\mathbf{\Gamma}$

$$B_p\left(\mathbf{k}_\parallel, E, V\right) = i\left[\mathbf{\Gamma}_p\left(\mathbf{k}_\parallel, z_+, V\right) - \mathbf{\Gamma}_p\left(\mathbf{k}_\parallel, z_-, V\right)\right] \tag{A.11}$$

and $z_\pm = E \pm i\delta$. The current is given by :

$$I(V) = \frac{e^2}{h}\frac{1}{N_\parallel}\sum_{\mathbf{k}_\parallel}\int_{\mu_R}^{\mu_L+V} T\left(\mathbf{k}_\parallel, E, V\right)\mathrm{d}E \tag{A.12}$$

A.2. Vertex correction

In this section we consider the same system as before, but the active N layers contains some disorder, the expression of the transmission coefficient obtained now by averaging over the disorder (hereafter $z_\pm \equiv \{\mathbf{k}_\parallel, E \pm i\delta, V\}$ and $a \equiv \{\mathbf{k}_\parallel, E, V\}$), i,e.

$$T\left(\mathbf{k}_\parallel, E, V\right) = \lim_{\delta\to0^+}\frac{1}{2}Tr\left\langle B_1(a)\,\mathbf{g}(z_+)\,B_N(a)\,\mathbf{g}(z_-) + B_1(a)\,\mathbf{g}(z_-)\,B_N(a)\,\mathbf{g}(z_+)\right\rangle. \tag{A.13}$$

The two leads are disorder-free, which means that both the self-energy $\mathbf{\Gamma}$ as well as the anti-hermitian part B remain the same as before (equations (A.7). and (A.11).), in this case the transmission coefficients are:

$$T\left(\mathbf{k}_\parallel, E, V\right) = \lim_{\delta\to0^+}\frac{1}{2}TrB_1(a)\left\langle\mathbf{g}(z_+)\,B_N(a)\,\mathbf{g}(z_-) + \mathbf{g}(z_-)\,B_N(a)\,\mathbf{g}(z_+)\right\rangle. \tag{A.14}$$

We follow here the same derivation done by Carva *et al* [39]

$$\left\langle\mathbf{g}(z_+)\,B(a)\,\mathbf{g}(z_-)\right\rangle = \bar{\mathbf{g}}(z_+)\,B(a)\,\bar{\mathbf{g}}(z_-) + \bar{\mathbf{g}}(z_+)\,\Gamma(z_+, z_-)\,\bar{\mathbf{g}}(z_-). \tag{A.15}$$

The transmission coefficient can decomposed into coherent transmission and uncoherent(vertex) transmission. The coherent transmission is expressed in term of the averaged auxiliary Green's function as

$$T_{\mathrm{coh}}\left(\mathbf{k}_\parallel, E, V\right) = \lim_{\delta\to0^+}\frac{1}{2}Tr\left[B_1(E)\,\bar{\mathbf{g}}(z_+)\,B_N(E)\,\bar{\mathbf{g}}(z_-) + B_1\bar{\mathbf{g}}(z_-)\,B_N(E)\,\bar{\mathbf{g}}(z_+)\right]. \tag{A.16}$$

The vertex contribution to the conductance is expressed in the same way like Carva, but instead of potential function P we take the potential function $\mathbf{P}_{RL}(z,V)$ and the Vertex-current is given by:

$$I_{\mathrm{VC}}(V) = \frac{e^2}{h}\int_{\mu_R}^{\mu_L+V}\mathrm{d}E\sum_{pLL'p'L_1L_2}\left[\bar{\mathbf{g}}B\bar{\mathbf{g}}\right]^{L'L}_{p}\mathbf{\Delta}^{LL'L_1L_2}_{pp'}\left(\mathbf{0}_\parallel, E, V\right)\left[\bar{\mathbf{g}}B\bar{\mathbf{g}}\right]^{L_1L_2}_{p'} \tag{A.17}$$

where

$$\left[\bar{\mathbf{g}}B\bar{\mathbf{g}}\right]^{L'L}_{p} = \frac{1}{N_\parallel}\sum_{\mathbf{k}_\parallel,L_1,L_2}\bar{\mathbf{g}}^{LL_1}_{p,1}(z_+)\,B^{L_1L_2}(a)\,\bar{\mathbf{g}}^{L_2L'}_{1,p}(z_-) \tag{A.18}$$

and

$$\boldsymbol{\Delta}_{pp'}^{LL'L_1L_2}\left(\mathbf{0}_{\parallel},E,V\right)=\delta_{p,p'}\left[\lambda_p^{-1}\left(E+i\delta,E-i\delta\right)\right]^{LL'L_1L_2}-\frac{1}{N_{\parallel}}\sum_{\mathbf{k}_{\parallel}}\overline{\mathbf{g}}_{p,p'}^{LL_1}\left(z_+\right)\overline{\mathbf{g}}_{p',p}^{L_2L'}\left(z_-\right) \tag{A.19}$$

where λ have the same expression as in the appendix of Carva *et al* [39]

The Total current now is expressed as the same of both coherent and vertex current,

$$I(V)=I_{\mathrm{VC}}(V)+\frac{e^2}{h}\frac{1}{N_{\parallel}}\sum_{\mathbf{k}_{\parallel}}\int_{\mu_R}^{\mu_L+V}T_{\mathrm{coh}}\left(\mathbf{k}_{\parallel},E,V\right)\mathrm{d}E. \tag{A.20}$$

ORCID iDs

Baadji Nadjib 0000-0002-0630-2398
Zanat Kamel 0000-0001-5662-9674

References

[1] Thapa A and Sharma B 2025 *Adv. Mater. Technol.* **10** e00133
[2] Si M, Cheng H Y, Ando T, Hu G and Ye P D 2021 *MRS Bull.* **46** 946–58
[3] Mao S 2007 *J. Nanosci. Nanotechnol.* **7** 1–12
[4] Wu K and He R 2025 *Nanotechnology* **36** 152501
[5] Leitao D C, Riel F J F v, Rasly M, Araujo P D R, Salvador M, Paz E and Koopmans B 2024 *npj Spintronics* **2** 54
[6] Butler W H, Zhang X G, Schulthess T C and MacLaren J M 2001 *Phys. Rev. B* **63** 054416
[7] Mathon J and Umerski A 2001 *Phys. Rev. B* **63** 220403
[8] Parkin S S P, Kaiser C, Panchula A, Rice P M, Hughes B, Samant M and Yang S H 2004 *Nat. Mater.* **3** 862–7
[9] Yuasa S, Nagahama T, Fukushima A, Suzuki Y and Ando K 2004 *Nat. Mater.* **3** 868–71
[10] Ikeda S, Hayakawa J, Ashizawa Y, Lee Y M, Miura K, Hasegawa H, Tsunoda M, Matsukura F and Ohno H 2008 *Appl. Phys. Lett.* **93** 082508
[11] Tan J, Yang G and Ouyang G 2024 *New J. Phys.* **26** 033047
[12] Tan J, Xu D, Ge M, Yang G and Ouyang G 2024 *Phys. Rev. B* **110** 125402
[13] Tusche C, Meyerheim H L, Jedrecy N, Renaud G and Kirschner J 2006 *Phys. Rev. B* **74** 195422
[14] Meyerheim H L, Popescu R, Jedrecy N, Vedpathak M, Sauvage-Simkin M, Pinchaux R, Heinrich B and Kirschner J 2002 *Phys. Rev. B* **65** 144433
[15] Luches P, Benedetti S, Liberati M, Boscherini F, Pronin I and Valeri S 2005 *Surf. Sci.* **583** 191–8
[16] Pal Singh J *et al* 2014 *Adv. Mater. Lett.* **5** 372–7
[17] Baadji N 2006 Étude ab-initio de magnétisme et du transport électronique dans les systémes hybrides (fer/semi-conducteur/fer) *PhD Thesis thése de doctorat dirigée par Dreyssé, Hugues Physique de la matiére condensée* Université Louis Pasteur (Strasbourg) (1971–2008) (available at: www.theses.fr/2006STR13263)
[18] Wang S, Ward R, Hesjedal T, Zhang X G, Wang C, Kohn A, Ma Q, Zhang J, Liu H and Han X 2012 *J. Nanosci. Nanotechnol.* **12** 1006–23
[19] Mezey L Z and Giber J 1982 *Jpn. J. Appl. Phys.* **21** 1569
[20] Overbury S, Bertrand P and Somorjai G 1975 *Chem. Rev.* **75** 547–60
[21] Tusche C, Meyerheim H L, Jedrecy N, Renaud G, Ernst A, Henk J, Bruno P and Kirschner J 2005 *Phys. Rev. Lett.* **95** 176101
[22] Młyńczak E, Freindl K, Spiridis N and Korecki J 2013 *J. Appl. Phys.* **113** 024320
[23] Miao G X, Park Y J, Moodera J S, Seibt M, Eilers G and Münzenberg M 2008 *Phys. Rev. Lett.* **100** 246803
[24] Mather P G, Read J C and Buhrman R A 2006 *Phys. Rev. B* **73** 205412
[25] Heiliger C, Zahn P, Yavorsky B Y and Mertig I 2006 *Phys. Rev. B* **73** 214441
[26] Ke Y, Xia K and Guo H 2010 *Phys. Rev. Lett.* **105** 236801
[27] Ozeki J, Itoh H and Inoue J 2007 *J. Magn. Magn. Mater.* **310** e644–5
[28] Zhang X G, Butler W H and Bandyopadhyay A 2003 *Phys. Rev. B* **68** 092402
[29] Kalitsov A, Zermatten P J, Bonell F, Gaudin G, Andrieu S, Tiusan C, Chshiev M and Velev J P 2013 *J. Phys.: Condens. Matter* **25** 496005
[30] Shen W, Mazumdar D, Zou X, Liu X, Schrag B D and Xiao G 2006 *Appl. Phys. Lett.* **88** 182508
[31] Boostan S E and Moradi H 2010 *J. Phys.: Conf. Ser.* **200** 052006
[32] Yang S H, Balke B, Papp C, Döring S, Berges U, Plucinski L, Westphal C, Schneider C M, Parkin S S P and Fadley C S 2011 *Phys. Rev. B* **84** 184410
[33] Wang Y, Zhang J, Zhang X G, Cheng H P and Han X F 2010 *Phys. Rev.* B **82** 054405
[34] Telesca D, Sinkovic B, Yang S H and Parkin S 2012 *J. Electron Spectrosc. Relat. Phenom.* **185** 133–9
[35] Baez Flores G G, van Schilfgaarde M and Belashchenko K D 2024 *Phys. Rev. B* **110** 224425
[36] Wortmann D, Bihlmayer G and Blügel S 2004 *J. Phys.: Condens. Matter* **16** S5819
[37] Rungger I, Mryasov O and Sanvito S 2009 *Phys. Rev. B* **79** 094414
[38] Turek I, Drchal V, Kudrnovsky J, Sob M and Weinberger P 2013 *Electronic Structure of Disordered Alloys, Surfaces and Interfaces* (Springer)
[39] Carva K, Turek I, Kudrnovský J and Bengone O 2006 *Phys. Rev. B* **73** 144421
[40] Andersen O K and Jepsen O 1984 *Phys. Rev. Lett.* **53** 2571–4
[41] Soven P 1967 *Phys. Rev.* **156** 809–13
[42] Taylor D W 1967 *Phys. Rev.* **156** 1017–29
[43] Velický B 1969 *Phys. Rev.* **184** 614–27

[44] Ke Y, Xia K and Guo H 2008 *Phys. Rev. Lett.* **100** 166805
[45] Meyerheim H L, Popescu R, Kirschner J, Jedrecy N, Sauvage-Simkin M, Heinrich B and Pinchaux R 2001 *Phys. Rev. Lett.* **87** 076102
[46] Turek I, Kudrnovský J and Drchal V 2000 Disordered alloys and their surfaces: The coherent potential approximation *Electronic Structure and Physical Properies of Solids ed H* Dreyssé (Springer) pp 349–78
[47] Belashchenko K D, Velev J and Tsymbal E Y 2005 *Phys. Rev. B* **72** 140404
[48] Zermatten P J, Gaudin G, Maris G, Miron M, Schuhl A, Tiusan C, Greullet F and Hehn M 2008 *Phys. Rev. B* **78** 033301
[49] Mavropoulos P, Papanikolaou N and Dederichs P H 2000 *Phys. Rev. Lett.* **85** 1088–91
[50] Tiusan C, Faure-Vincent J, Bellouard C, Hehn M, Jouguelet E and Schuhl A 2004 *Phys. Rev. Lett.* **93** 106602
[51] Bonell F, Andrieu S, Bataille A M, Tiusan C and Lengaigne G 2009 *Phys. Rev. B* **79** 224405
[52] Nawa K, Masuda K and Miura Y 2021 *Phys. Rev. Appl.* **16** 044037
[53] pu Wang Y, jun Qiu J, Lu H, Yap Q J, Wang W, Han G, Ngo D T and Teo K L 2013 *2013 IEEE 5th Int. Nanoelectronics Conf. (INEC)* pp 215–8
[54] Garg C *et al* 2025 *Nat. Nanotechnol.* **20** 360–5
[55] Jiang L N, Chi B Y and Han X F 2025 *Phys. Rev. B* **111** 224422